Title

Water-Dissociation Catalysis Near the Reversible Limit in Bipolar Membrane Electrolyzers

Authors

Boettcher, Shannon
Chen, Lihaokun
Sarma, Prasad
et al.

Publication Date

2023

DOI

10.21203/rs.3.rs-3447094/v1

nature materials

Article

https://doi.org/10.1038/s41563-024-01943-8

Materials descriptors for advanced water dissociation catalysts in bipolar membranes

Received: 14 October 2023

Accepted: 5 June 2024

Published online: 01 July 2024

Check for updates

Sayantan Sasmal[1], Lihaokun Chen[1,2,3], Prasad V. Sarma[1], Olivia T. Vulpin[1], Casey R. Simons[4], Kacie M. Wells[5], Richard J. Spontak[6] & Shannon W. Boettcher[1,2,3]

The voltage penalty driving water dissociation (WD) at high current density is a major obstacle in the commercialization of bipolar membrane (BPM) technology for energy devices. Here we show that three materials descriptors, that is, electrical conductivity, microscopic surface area and (nominal) surface-hydroxyl coverage, effectively control the kinetics of WD in BPMs. Using these descriptors and optimizing mass loading, we design new earth-abundant WD catalysts based on nanoparticle SnO_2 synthesized at low temperature with high conductivity and hydroxyl coverage. These catalysts exhibit exceptional performance in a BPM electrolyser with low WD overvoltage (η_{wd}) of 100 ± 20 mV at 1.0 A cm^{-2}. The new catalyst works equivalently well with hydrocarbon proton-exchange layers as it does with fluorocarbon-based Nafion, thus providing pathways to commercializing advanced BPMs for a broad array of electrolysis, fuel-cell and electrodialysis applications.

Water dissociation (WD, $H_2O \rightarrow H^+ + OH^-$) is a fundamental chemical reaction that occurs across many technologies and electrochemical processes. Bipolar membranes (BPMs), first reported as early as 1956[1], can be used to drive and study WD. They consist of a polymeric cation-exchange layer (CEL) that selectively conducts cations, laminated with an anion-exchange layer (AEL) that selectively conducts anions[2,3] (Fig. 1). With an applied current/voltage that moves H^+ and OH^- out of the BPM in opposite directions (Fig. 1b), BPMs dissociate water and, thus, transduce electric energy into chemical energy in the form of a difference in proton chemical potential (that is, a pH gradient). BPMs are used today in small-scale commercial applications for onsite acid–base synthesis, metals recycling and food processing[4,5]. To use them in large-scale applications for energy devices such as water[6–9], seawater[10] and CO_2 (refs. 11–14) electrolysers, hydrogen fuel cells[15,16] and carbon-capture devices[17], they must operate at high currents to lower amortized capital expense (typically ≥1 A cm^{-2}) and with good voltage efficiencies (probably <100 mV loss driving WD) to lower electricity operating expense. Meeting these metrics requires efficient catalysts at the AEL|CEL junction to eliminate the WD overvoltage (η_{wd}), which is the free-energy loss associated with driving $H_2O \rightarrow H^+ + OH^-$ and separating the incipient protons and hydroxides[18]. While there has been progress in designing new WD catalysts, primarily consisting of metal-oxide nanoparticles[6,7,19,20] or graphene oxides[21], and in building three-dimensional BPM junctions[22,23], no BPM so far has exhibited sufficient performance characteristics for these broader energy applications. This shortcoming is, in part, due to the lack of understanding how the WD reaction is catalysed by materials surfaces and of the materials design rules for constructing effective catalysed junctions.

In a BPM, the coverage or thickness of the WD catalyst layer located between the CEL and AEL modulates η_{wd}, with full coverage being optimal for graphene oxide[21] and the optimal thickness depending on the electronic properties of metal-oxide catalysts[6] (Fig. 1b). High-dielectric

[1]Department of Chemistry & Biochemistry and the Oregon Center for Electrochemistry, University of Oregon, Eugene, OR, USA. [2]Department of Chemical & Biomolecular Engineering and Department of Chemistry, University of California, Berkeley, CA, USA. [3]Energy Storage and Distributed Resources Division, Lawrence Berkeley National Laboratory, Berkeley, CA, USA. [4]Center for Materials Characterization in Oregon, University of Oregon, Eugene, OR, USA. [5]Fiber and Polymer Science Program, North Carolina State University, Raleigh, NC, USA. [6]Departments of Chemical & Biomolecular Engineering and Materials Science & Engineering and Department of Materials Science & Engineering, North Carolina State University, Raleigh, NC, USA.
e-mail: boettcher@berkeley.edu

https://doi.org/10.1038/s41563-024-01943-8

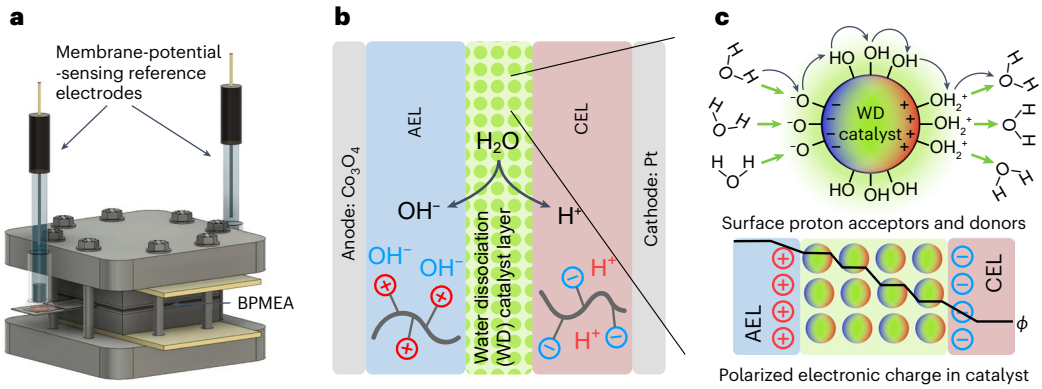

Fig. 1 | Membrane-potential sensing in a BPM electrode assembly (BPMEA) driving WD. a, Schematic of MEA and electrolyser with reference electrodes. Pure water is circulated to both the cathode and anode side to feed the BPM junction through the gas-diffusion and ionomer layers. The WD process occurs at the CEL|AEL junction, and CEL and AEL membrane strips are used to connect external reference electrodes. The voltage between the two reference electrodes is recorded as a function of the applied current, and $V_{ref} - V_{ref}^{eq}$ is taken as η_{wd} when *iR* voltage drops through the AEL and CEL are small. **b**, Water is dissociated at the BPM junction with the aid of a catalyst laminated at the AEL|CEL junction, and the formed H^+ and OH^- are separated by the gradients in electrochemical potential. **c**, The local electric field is thought to orient water molecules and facilitate the proton transfer to/from the surface of the oxide WD catalysts. Plausible electric-field screening from mobile electronic charges inside the WD particles is illustrated by a schematic electric-potential ϕ profile across the BPM junction.

nanoparticles measuring 20–30 nm in diameter, such as anatase or rutile TiO_2, tend to possess a narrow optimal range with catalyst layer thicknesses of ca. 200–300 nm, while for electronically conductive WD catalysts, such as IrO_2, thicker layers with higher loading are more effective[6]. The acid–base properties of the metal oxides, as reflected in part by the pH of zero charge (PZC), also seem to be important; bilayers of basic PZC oxides in contact with the AEL and acidic PZC oxides in contact with the CEL tend to work better than single-component WD catalyst layers[8]. Temperature-dependent BPM WD kinetics measurements where η_{wd} is isolated using two membrane-potential-sensing reference electrodes reveal that the applied voltage increases the rate of WD not by decreasing the activation energy for WD (which is commonly predicted[24–26] by the application of Onsager's model of the Wien effect) but by increasing the kinetic pre-factor, which was interpreted in terms of a water pre-organization hypothesis[19,27]. Continuum simulations established that metal or graphene oxides acting as proton donors or acceptors are probably central to low-voltage BPM operation[21,24].

Despite these advances, it is still unclear how exactly to design better WD catalysts. The best catalysts, such as IrO_2, TiO_2, graphene oxide or bilayers of oxides, still all yield η_{wd} values that are 200–300 mV at ~0.5 A cm^{-2}, a low current for an energy device[6,8,21]. While these are suitable for niche applications and are superior to commercial BPMs, the capital and operating cost (electricity expenditures) drive requirements for energy devices to function at higher currents of ≥1 A cm^{-2} with high efficiency and small η_{wd}. A further challenge is that many of the newer most promising BPMs reported use of Nafion—a perfluorinated ionomer—as the CEL, in which case health, environmental, cost and sustainability concerns might limit their deployment[28].

Here, we apply an experiment-driven materials-descriptors approach to create advanced WD catalysts and BPMs with unprecedented voltage efficiency using both Nafion and fully hydrocarbon CELs. We measured hypothesized materials properties of nine catalyst-particle compositions including (1) ex situ electronic conductivity (thought to affect electric field screening), (2) gas-adsorption surface area (SA; expected to scale with the number of active sites) and (3) surface-hydroxyl population (nominal water-adsorption sites). We mapped these properties with η_{wd} at the optimal loading and thickness, independently determined for each catalyst, and found that the electrical conductivity and SA-normalized adsorbed water and hydroxyl quantity are most strongly correlated with η_{wd}. Using these as design parameters, we created a new WD catalyst synthesized by the low-temperature hydrolysis of $SnCl_4$ without subsequent calcination. The resultant nanoparticle SnO_2 catalysts possess both higher electronic conductivity and higher surface-adsorbed water and hydroxyl content than benchmark P25-TiO_2 nanoparticles, leading to substantially faster kinetics for WD in the BPM.

Pure-water electrolysers fabricated from these BPMs operate at 1.0 A cm^{-2} at 2.1 V and 55 °C, quantitatively matching the best electrolysers that can be fabricated using the same alkaline-exchange membranes (whose performance is limited by the oxidative instability of the anode ionomer[29]). Membrane-sensing experiments show that this performance is attributed to a low η_{wd} of 100 ± 20 mV at 1.0 A cm^{-2} and 55 °C and an apparent WD activation energy ($E_{a,wd}$) of 18 ± 2 kJ mol^{-1}, which is below that of the nanoparticle TiO_2 benchmark (~25–30 kJ mol^{-1})[6]. Degradation rates of ~87 μV h^{-1} in BPM WD performance are observed over 100 h at 1.0 A cm^{-2}, without optimization. By modifying the catalyst-deposition procedure, the new SnO_2 WD catalysts were then used to construct hydrocarbon BPMs, fabricated from either a sulfonated poly(ether-ether ketone) (SPEEK) or a midblock-sulfonated poly[*tert*-butylstyrene-*b*-(ethylene-*alt*-propylene)-*b*-styrene-*b*-(ethylene-*alt*-propylene)-*b*-*tert*-butylstyrene] (TESET) pentablock polymer[30] to replace the Nafion CEL, with no performance difference ($\eta_{wd} \approx 100$ mV at 1.0 A cm^{-2} and 55 °C). These BPM water electrolysers (BPMWEs) provide locally acidic conditions at the H_2 evolving cathode that (1) dramatically speed the kinetics compared with alkaline conditions, (2) enable a ~20× reduction in cathode Pt loading and (3) afford use of an earth-abundant Co_3O_4 and related catalysts at the locally basic anode. These advanced BPMs also efficiently work in proof-of-concept electrodialysis environments driving WD with acid and base contacting the CEL and AEL, respectively.

Materials descriptors for catalysing heterogeneous WD

The precise measurement of WD kinetics and overpotential is non-trivial. In electrochemical reactions, WD is coupled with other reaction steps, such as for alkaline hydrogen evolution where water is the proton source and must be dissociated ($2H_2O + 2e^- \rightarrow H_2 + 2OH^-$)[31]. The BPM dissociates water at the AEL|CEL interface, but nearly all BPM measurements are performed in H-cells with acid, base or salt supporting electrolytes on either side of the BPM and two reference electrodes placed exterior to the BPM to measure the nominal transmembrane voltage changes upon polarization. This method is imprecise because a portion of the current is always carried by species other than OH^- and H^+ (that is, co-ions)[32], pH gradients develop upon polarization in salt

https://doi.org/10.1038/s41563-024-01943-8

supporting electrolytes[33] and, if dissimilar electrolytes such as acid and base are used, the equilibrium transmembrane voltage is affected by spontaneous acid–base recombination[34]. We previously reported a membrane–electrode assembly (MEA) electrolyser platform for the measurement of WD kinetics in the absence of these convoluting effects[8,19]. The electrolyser platform and use of dual membrane reference electrodes also eliminate the obfuscating junction potentials that may change with time and current when separate electrolytes are contacted the BPM using a more typical four-probe approach and H-cell[22].

Anode and cathode active layers are sprayed from inks containing dispersed or dissolved ionomer and catalyst powders onto porous transport layers, as in a fuel cell or membrane electrolyser, with the BPM sandwiched between them under static compression in a test cell (Fig. 1a). Pure water is fed to the system, and polarization curves in electrolysis mode (that is, reverse bias driving WD) or, in principle, fuel-cell mode (that is, forward bias driving H^+/OH^- recombination[35]), are measured with H^+ and OH^- as the only mobile ionic charge carriers. We integrate two reference electrodes, one connected to the CEL and the other to the AEL, using the membrane-potential-sensing geometry[36] to directly extract the fraction of the applied voltage driving WD[19] relative to anode and cathode losses. The value of η_{wd} is taken as the magnitude of the electrostatic potential change across the BPM junction as a function of current density relative to its equilibrium value[8,19]. The equilibrium value is the voltage measured across the BPM under open-circuit conditions, approaching its thermodynamic value in the absence of current.

A range of commercial metal-oxide nanoparticles expected to be chemically stable in both strong base (as is present at the AEL surface) and strong acid (as is present at the CEL surface) were selected for understanding the materials descriptors. For each catalyst, a series of BPMs were fabricated with different mass loading (thicknesses) of the nanoparticle catalyst layers, and the optimal thickness of each catalyst was determined (Supplementary Fig. 1). Consistent with our previous studies[6,8], the optimal loading was 20–200 μg cm^{-2} for semiconducting oxide particles including various forms of TiO_2 and nominally undoped SnO_2. The optimal loading levels for the electrically conductive Sb:SnO_2 and IrO_2 particles were larger (300–1,000 μg cm^{-2}), probably because these WD catalysts screen and focus the electric field in the BPM junction[6]. For each sample, the electrical conductivity (σ) was estimated from a two-probe current–voltage measurement of an unsintered disk of the nanoparticle powder held under static pressure at ~1,000 psi between two stainless-steel cylinders.

Oxide nanoparticles are thought to catalyse WD via a mechanism that involves at least three steps[19]: (1) proton transfer to the surface from water to form free OH^-, (2) proton transport across the surface and (3) proton transfer from the surface to water to form free H_3O^+ (Fig. 1c). For this mechanism to be fast, the surface of the metal oxide needs a large coverage of proton adsorption and donor sites. Because water typically dissociates into adsorbed hydroxyls on pristine metal-oxide surfaces[37,38], we measured the nominal surface concentration of hydroxyls or, equivalently, sites for strong surface-water adsorption (which are indistinguishable by thermal gravimetric analysis)[39]. Generally, two thermal gravimetric analysis mass-loss regions are observed: one at low temperatures assigned to dehydration and the other at higher temperatures thought to reflect dehydroxylation[39]. The nominal total hydroxyl content (C_{OH} in mol g^{-1}) is calculated by $C_{OH} = \frac{2}{18}(|w_1 - w_2|)/w_1$, assuming the mass change is predominantly given by 2 (M–OH) → (M–O–M) + H_2O. Here, w_2 is the mass of the sample at final temperature (~490 °C), and w_1 is the mass of the sample after dehydration at 120 °C for 10 min. The differences between bridging and terminal hydroxyl groups in the oxide nanoparticles were ascertained from solid-state ^{1}H NMR spectra[40], but the distinction was not found useful to predict WD properties in any simple way (see below). The Brunauer–Emmett–Teller microscopic SA of each sample was obtained either from the particle manufacturer or calculated from N_2 absorption isotherms.

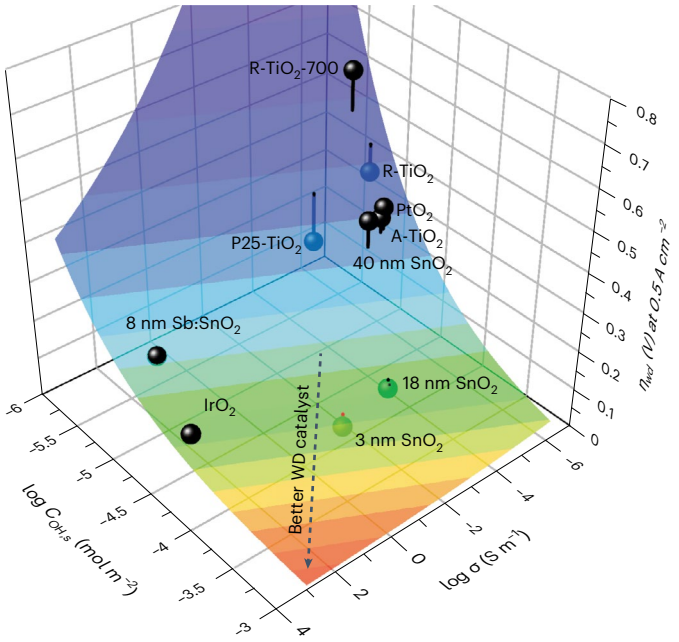

Fig. 2 | Materials design for advanced water-dissociation catalysts. Contour plot of η_{wd} upon changing σ and $C_{OH,s}$. The colour gradient along the z axis corresponds to the predicted η_{wd} at 500 mA cm^{-2}. The spherical markers are the experimental η_{wd} at 500 mA cm^{-2}. The vertical distance between experimental (spheres) and predicted η_{wd} (coloured surface) illustrates the goodness of fit. The dotted line along the colour gradient indicates the path to achieving WD catalysts with lower η_{wd}. The red dot shows the exceptional performance of the 3 nm SnO_2. Two-dimensional plots for η_{wd} at 0.5 A cm^{-2} upon changing $C_{OH,s}$ and σ are provided in Supplementary Fig. 7. Although these analyses were performed at 500 mA cm^{-2}, η_{wd} for the oxide-nanoparticle-catalysed materials varies nearly linearly with current (that is, we find a roughly constant WD resistance) so these correlations persist over a range of currents, as described in Supplementary Information.

A multivariant linear-regression fit of the measured η_{wd} (at optimal mass loading for 500 mA cm^{-2}) versus the measured conductivity (σ), SA and hydroxyl concentration (C_{OH}) was performed (with IBM SPSS software; Supplementary Fig. 3a). This analysis revealed that C_{OH}, SA and σ modulate η_{wd} according to the empirical relationship

$$\eta_{wd} \propto \left(\frac{\sigma}{\mathrm{S\,m^{-1}}}\right)^{-0.06} \times \left(\frac{C_{OH}}{\mathrm{mol\,g^{-1}}}\right)^{-0.47} \times \left(\frac{SA}{\mathrm{m^2\,g^{-1}}}\right)^{0.36}. \quad (1)$$

This fit ($R^2 = 0.94$, $R^2_{adjusted} = 0.90$) predicts that SA is directly related to η_{wd}, which is surprising as we expected higher SA to lead to lower η_{wd}. However, we found that C_{OH} and σ are strongly cross correlated with SA (Supplementary Fig. 3b) and, thus, have effects on η_{wd} that are inseparable by this analysis. We thus defined a new parameter (Supplementary Discussion), the SA-normalized total-hydroxyl content given by $C_{OH,s} = C_{OH}/SA$. With this parameter, no intercorrelated predictors are observed, and a similarly good empirical fit was obtained ($R^2 = 0.93$, $R^2_{adjusted} = 0.91$; Supplementary Fig. 3c).

$$\eta_{wd} \propto \left(\frac{\sigma}{\mathrm{S\,m^{-1}}}\right)^{-0.07} \times \left(\frac{C_{OH,s}}{\mathrm{mol\,m^{-2}}}\right)^{-0.48} \quad (2)$$

It is useful to consider why a regression using $C_{OH,s}$ provides a good fit, as it predicts the (non-physical) outcome that minimizing SA lowers η_{wd} by maximizing $C_{OH,s}$. The term $C_{OH,s}$, however, is a measure of how closely packed the nominal surface hydroxyls are on the oxide nanoparticle surfaces. We proposed, on the basis of voltage-dependent kinetic data, that WD requires not only efficient proton transfer to and

https://doi.org/10.1038/s41563-024-01943-8

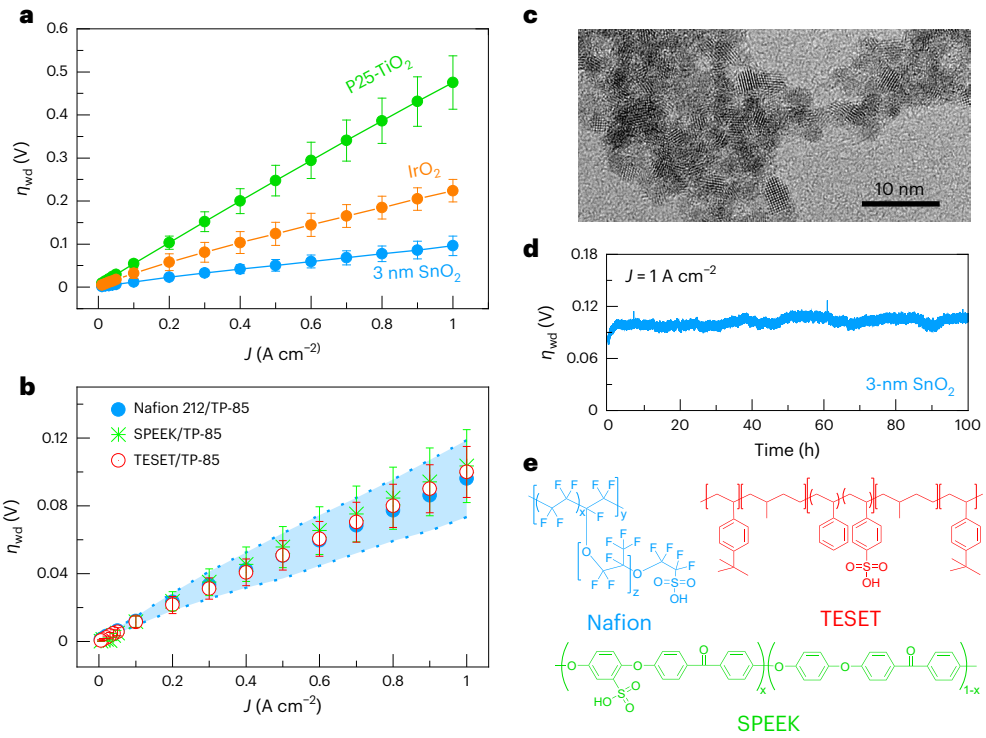

Fig. 3 | Advanced WD catalysts in hydrocarbon and fluorocarbon BPMs. **a**, WD polarization curves for BPMs with different catalysts. The new 3 nm SnO_2 WD catalyst provides $\eta_{wd} \approx 100$ mV at 1.0 A cm^{-2}. **b**, WD polarization curves for BPMs with Nafion NR212 compared with SPEEK and TESET ionomers as the CEL. PiperION-A40-HCO_3 (TP-85) was used as the AEM in all cases. Optimized WD catalyst loading was used in each experiment shown. The η_{wd} in the case of hydrocarbon-based BPMs falls within the error band of Nafion-based BPMs. This result demonstrates that fluorinated ionomers are not needed in advanced BPMs. The ion-exchange capacity (IEC) values of the tested CELs are 1.06, 1.78 and 2.0 mmol g^{-1} (within the limit of the experimental error), respectively, for the Nafion, SPEEK and TESET. The consistent performance across all CELs, despite their different IEC values, suggests that WD catalysts are more crucial than the exact magnitude of the interfacial electric field. **c**, Transmission electron microscopy micrograph of 3 nm SnO_2. **d**, Chronopotentiometric *V*–*t* curve at 1.0 A cm^{-2} using 3 nm SnO_2 over 100 h with a nominal degradation rate of ~87 μV h^{-1}. **e**, Chemical structures of different CELs used in this study. The data points in **a** and **b** are obtained from the average of three devices, with the error bars representing plus or minus one standard deviation.

from water, but also proton hopping across the surface of the oxide, because when a particle is polarized in an electric field, the fastest sites for accepting protons from water are not the same as those for donating protons to water[19]. It is thus conceivable that $C_{OH,s}$ is related to the efficacy of this hopping process. We also emphasize that low-SA oxide particles (that is, larger than ~100 nm in diameter) were not studied here as they are not viable for processing into reproducible BPMs, and we do not expect such low-SA catalysts to function effectively. The correlation in equation (2) thus probably only holds across nominally high-SA powders. A multivariant linear regression without SA (Supplementary Fig. 5) was also assessed, and the correlation drops significantly.

Figure 2 displays the predicted η_{wd} from equation (2) (represented as the coloured surface) compared with the experimental η_{wd} at 500 mA cm^{-2} (represented by spheres). Using this analysis, we compare specific catalysts of interest. For example, 30 nm R-TiO_2 was heated in H_2 at 700 °C to introduce H-defects as n-type dopants[41] and, thus, increase σ, but the treated sample R-TiO_2-700 also exhibited an order-of-magnitude lower $C_{OH,s}$ and worse WD performance (Supplementary Fig. 8b). Solid-state ^{1}H NMR analysis shows a large change in total hydroxyl content compared with the pristine sample (Supplementary Fig. 8c,d). Both 18 nm SnO_2 and high-SA IrO_2 possess similar WD performance (Supplementary Table 3), despite six-orders-of-magnitude higher conductivity for IrO_2, which is offset by the three times higher $C_{OH,s}$ of 18 nm SnO_2 than IrO_2. Likewise, 8 nm Sb:SnO_2 yields much higher η_{wd} than 18 nm SnO_2, despite having five-orders-higher conductivity than 18 nm SnO_2, because the 8 nm Sb:SnO_2 has ~14 times lower $C_{OH,s}$ than 18 nm SnO_2 (Supplementary Table 3). These results are consistent with a mechanism whereby high-σ catalysts focus the electric field to the WD reactions sites, whereas high $C_{OH,s}$ facilitates proton transfer to and from water and proton hopping across the catalyst. All these results are consistent with both conductivity and surface hydroxyl coverage being key to achieving fast WD.

Descriptor-based design of WD catalysts

To develop advanced WD catalysts, our analysis suggests one should target oxides with high conductivity and surface-hydroxyl coverage (Fig. 2). Yet, usually higher σ is obtained by high-temperature processes that reduce surface hydroxyl coverage. New WD catalyst should also be produced from inexpensive oxides with chemical stability in strong acid and base, in which case precious metals, like Pt, or semi-metallic oxides, like IrO_2 and RuO_2, are probably not viable.

Given these descriptors and constraints, we targeted tin-oxide-based WD catalysts. Using an inexpensive $SnCl_4$ precursor, we synthesized ~3 nm SnO_2 nanoparticles via low-temperature hydrolysis in water following established procedures[42]. The particles have ~50 times higher electrical conductivity than the larger 18 nm SnO_2 commercial nanopowder (42 versus 0.8 mS m^{-1}), presumably due to defects associated with the low-temperature synthesis route. This 3 nm SnO_2 (Fig. 3c) is directly isolated from water and never heated above 100 °C and, thus, simultaneously exhibits (slightly) higher C_{OH} (1×10^{-2} versus 7×10^{-3} mol g^{-1}) and similar $C_{OH,s}$ (1×10^{-4} mol m^{-2}), while providing nearly double the SA compared with commercial 18 nm SnO_2 (102 versus 60 m^2 g^{-1}).

The new 3 nm SnO_2 possesses exceptional WD activity (Fig. 3a). With an optimal loading of 30 μg cm^{-2}, the 3 nm SnO_2 catalyst

sandwiched between Nafion NR212 CEL and Piperion TP-85 AEL yields η_{wd} values of ~50 mV at 500 mA cm^{-2} and ~100 mV at 1.0 A cm^{-2} (Fig. 3a). Such BPM WD performance is unprecedented. The new advanced BPMs have ~50 times better voltage performance than Fumasep ($\eta_{wd} \approx 100$ mV at 20 mA cm^{-2})[8], are approximately two to three times better than our best previous bilayer WD catalysts ($\eta_{wd} > 200$ mV at 1 A cm^{-2}) that required expensive IrO_2, and are approximately five times better than our simpler benchmark P25-TiO_2 (Fig. 3a) owing to a lower (apparent) activation energy $E_{a,wd}$ of 18 ± 2 kJ mol^{-1} (Supplementary Fig. 11) compared with 25–30 kJ mol^{-1} for P25-TiO_2. While the low activation energy for the new SnO_2 catalyst is one key to enhanced performance, we cannot yet provide a mechanistic explanation for this effect beyond previously published ideas[19,27].

We measured η_{wd} for the 3 nm SnO_2 at 1.0 A cm^{-2} for 100 h (Fig. 3d) and found minimal degradation (~87 μV h^{-1}), consistent with the fact that there is a small (non-equilibrium) voltage across the AEL|CEL junction (that is, $\eta_{wd} \approx 100$ mV) and the local pH extrema set by the AEL and CEL are within the chemical stability window of SnO_2. The 3 nm SnO_2 WD catalyst was then used to fabricate BPMs based on two different hydrocarbon polymers (Fig. 3e): a sulfonated poly(ether-ether ketone) (SPEEK, manufactured by eSpin Technologies) and a midblock-sulfonated pentablock polymer (TESET, manufactured by Kraton Corporation and solvent-cast from a toluene–isopropanol co-solvent) to replace the Nafion CEL, with no performance difference (Fig. 3b shows $\eta_{wd} \approx 100$ mV at 1.0 A cm^{-2} and 55 °C).

BPM device prototypes

The new 3 nm SnO_2 WD catalyst enables BPMs to reach performance levels suitable for use in high-current-density energy devices. Using 3 nm SnO_2 as the WD catalyst, Co_3O_4 as the oxygen evolution reaction (OER) catalyst, and Pt as the hydrogen evolution reaction (HER) catalyst provides electrolysis performance that is better than reference alkaline exchange membrane (AEM) electrolysers fabricated from the same AEM ionomer and electrocatalysts (Fig. 4a). This is possible because the HER, even on Pt, is ~100 times slower in alkaline than in acidic electrolyte[43]. The BPMWE uses more voltage to drive the additional WD and ohmic losses compared with the AEMWE, but the AEMWE must drive HER on Pt in an unfavorable alkaline local ionomer environment. To intentionally emphasize this difference, we reduced the Pt loading at the cathode from 2.0 to 0.1 mg cm^{-2} for both the BPMWE and the AEMWE (Fig. 4a). The BPMWE driving HER in a locally acidic environment exhibited almost no change in performance, while the AEMWE voltage increased by ~150 mV. We note that the performance gap is emphasized here by the use of Pt HER catalysts instead of Pt-Ru alloys that have four to five times higher alkaline HER performance[44]. These results show the opportunities created by local pH control via the BPM.

Another important application of BPMs is in electrodialysis to generate acid and base. Inexpensive strong base, such as aqueous KOH, is critical to implementing viable schemes to capture CO_2 from the air or ocean. Today's commercial BPM electrodialysis (BPMED) systems[45] typically operate at 50–100 mA cm^{-2}, limited in part by the lack of efficient BPMs for higher current operation. A common commercial BPM, ASTOM BP-1E (Neosepta)[46], drives WD with $\eta_{wd} \approx 0.4$ V at 100 mA cm^{-2}. By combining the new 3 nm SnO_2 WD catalyst with asymmetric pH feeds (0.1 M H_2SO_4 and 0.1 M KOH), we demonstrate a BPM driving WD in electrodialysis-like conditions (Fig. 4b) with 40 times lower $\eta_{wd} \approx 0.16$ V at 1.0 A cm^{-2}. This test simulates the environment near the BPM within an electrodialysis system with differential pH acid–base feed but is not a complete BPMED device. These experimental proof-of-concept devices demonstrate the WD catalysis capability of the 3 nm SnO_2 under differential pH conditions as in a BPMED assembly (Supplementary Fig. 18) as well as in pure-water electrolysis. Further electrodialysis cell engineering is required to demonstrate advanced BPMs operating in electrodialysis cells at these high current densities.

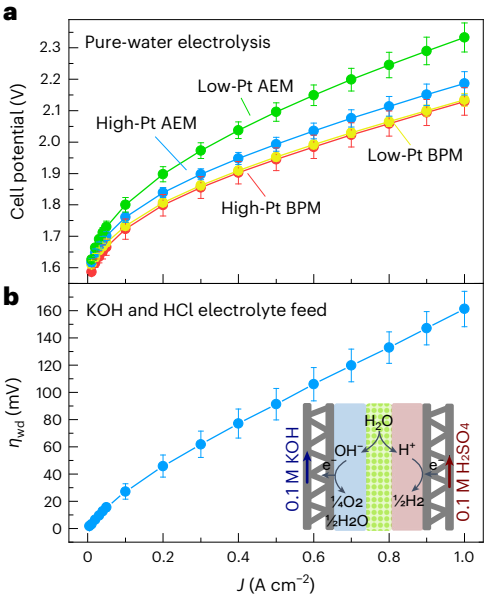

Fig. 4 | Advanced BPMWE and electrodialysis devices. a, Polarization curves of optimized BPM and AEM electrolysers with low and high Pt loading. The error bars represent one standard deviation on the reported average for three different devices fabricated with the catalyst loading indicated. For the three devices at each loading, the CEL was Nafion 212, SPEEK and TESET (one device each) and the AEL was TP-85 for all. Pure DI water was fed into both the electrolysers. All conditions, including catalysts, temperature and electrode catalyst loadings, were the same in both BPMWE and AEMWE. BPMWE reveals higher performance due to the fast kinetics of acidic HER but is not competitive on performance yet compared with proton-exchange-membrane electrolysers using IrO_2 (Supplementary Discussion and Data). The cell was operated at atmospheric pressure on both the anode and cathode and the flow rate was 200 ml min^{-1}. **b**, Polarization curve for BPM with 3 nm SnO_2 WD catalyst where aqueous 0.10 M H_2SO_4 and 0.10 M KOH were fed to the cathode and anode, respectively, mimicking a BPMED environment[47]. The inset displays the test architecture with acid and base feed. The data points in **a** and **b** are obtained from the average of three devices, with the error bars representing plus or minus one standard deviation.

The foundational understanding reported here, coupled with the success in achieving WD catalysis with low η_{wd} (near thermodynamic reversibility) and demonstration of high-performance prototype devices using non-fluorinated components, is expected to drive continued innovation and application of BPM devices across emerging energy technologies, in addition to improving the existing applications wherein BPMs are currently used.

Online content

Any methods, additional references, Nature Portfolio reporting summaries, source data, extended data, supplementary information, acknowledgements, peer review information; details of author contributions and competing interests; and statements of data and code availability are available at https://doi.org/10.1038/s41563-024-01943-8.

References

1. Frilette, V. J. Preparation and characterization of bipolar ion exchange membranes. *J. Phys. Chem.* **60**, 435–439 (1956).
2. Pärnamäe, R. et al. Bipolar membranes: a review on principles, latest developments, and applications. *J. Membr. Sci.* **617**, 118538 (2021).
3. Giesbrecht, P. K. & Freund, M. S. Recent advances in bipolar membrane design and applications. *Chem. Mater.* **32**, 8060–8090 (2020).
4. Arana Juve, J.-M., Christensen, F. M. S., Wang, Y. & Wei, Z. Electrodialysis for metal removal and recovery: a review. *Chem. Eng. J.* **435**, 134857 (2022).

5. Bazinet, L., Lamarche, F. & Ippersiel, D. Bipolar-membrane electrodialysis: applications of electrodialysis in the food industry. *Trends Food Sci. Technol.* **9**, 107–113 (1998).
6. Chen, L., Xu, Q., Oener, S. Z., Fabrizio, K. & Boettcher, S. W. Design principles for water dissociation catalysts in high-performance bipolar membranes. *Nat. Commun.* **13**, 3846–3846 (2022).
7. Oener, S. Z., Twight, L. P., Lindquist, G. A. & Boettcher, S. W. Thin cation-exchange layers enable high-current-density bipolar membrane electrolyzers via improved water transport. *ACS Energy Lett.* **6**, 1–8 (2020).
8. Oener, S. Z., Foster, M. J. & Boettcher, S. W. Accelerating water dissociation in bipolar membranes and for electrocatalysis. *Science* **369**, 1099–1103 (2020).
9. Ge, Z. et al. High-performance bipolar membrane for electrochemical water electrolysis. *J. Membr. Sci.* **656**, 120660 (2022).
10. Marin, D. H. et al. Hydrogen production with seawater-resilient bipolar membrane electrolyzers. *Joule* **7**, 765–781 (2023).
11. Xie, K. et al. Bipolar membrane electrolyzers enable high single-pass CO_2 electroreduction to multicarbon products. *Nat. Commun.* **13**, 3609–3609 (2022).
12. Li, Y. C. et al. Bipolar membranes inhibit product crossover in CO_2 electrolysis cells. *Adv. Sustain. Syst.* **2**, 1700187 (2018).
13. Salvatore, D. A. et al. Electrolysis of gaseous CO_2 to CO in a flow cell with a bipolar membrane. *ACS Energy Lett.* **3**, 149–154 (2017).
14. Disch, J., Ingenhoven, S. & Vierrath, S. Bipolar membrane with porous anion exchange layer for efficient and long-term stable electrochemical reduction of CO_2 to CO. *Adv. Energy Mater.* **13**, 2301614 (2023).
15. Li, Q. et al. Theoretical design strategies of bipolar membrane fuel cell with enhanced self-humidification behavior. *J. Power Sources* **307**, 358–367 (2016).
16. Ünlü, M., Zhou, J. & Kohl, P. A. Hybrid anion and proton exchange membrane fuel cells. *J. Phys. Chem. C* **113**, 11416–11423 (2009).
17. Bui, J. C. et al. Analysis of bipolar membranes for electrochemical CO_2 capture from air and oceanwater. *Energy Environ. Sci.* **16**, 5076–5095 (2023).
18. Bui, J. C. et al. Multi-scale physics of bipolar membranes in electrochemical processes. *Nat. Chem. Eng.* **1**, 45–60 (2024).
19. Chen, L., Xu, Q. & Boettcher, S. W. Kinetics and mechanism of heterogeneous voltage-driven water-dissociation catalysis. *Joule* **7**, 1867–1886 (2023).
20. Shehzad, M. A. et al. Shielded goethite catalyst that enables fast water dissociation in bipolar membranes. *Nat. Commun.* **12**, 9 (2021).
21. Lucas, É. et al. Asymmetric bipolar membrane for high current density electrodialysis operation with exceptional stability. Preprint at https://chemrxiv.org/engage/chemrxiv/article-details/642df4da0784a63aee99154d (2023).
22. Powers, D. et al. Freestanding bipolar membranes with an electrospun junction for high current density water splitting. *ACS Appl. Mater. Interfaces* **14**, 36092–36104 (2022).
23. Kole, S. et al. Bipolar membrane polarization behavior with systematically varied interfacial areas in the junction region. *J. Mater. Chem. A* **9**, 2223–2238 (2021).
24. Bui, J. C., Corpus, K. R. M., Bell, A. T. & Weber, A. Z. On the nature of field-enhanced water dissociation in bipolar membranes. *J. Phys. Chem. C* **125**, 24974–24987 (2021).
25. Cai, J. et al. Wien effect in interfacial water dissociation through proton-permeable graphene electrodes. *Nat. Commun.* **13**, 5776–5776 (2022).
26. Onsager, L. Deviations from Ohm's law in weak electrolytes. *J. Chem. Phys.* **2**, 599–615 (1934).
27. Rodellar, C. G., Gisbert-Gonzalez, J. M., Sarabia, F., Roldan Cuenya, B. & Oener, S. Z. Ion solvation kinetics in bipolar membranes and at electrolyte–metal interfaces. *Nat. Energy* 10.1038/s41560-41024-01484-z (2024).
28. Henry, B. J. et al. A critical review of the application of polymer of low concern and regulatory criteria to fluoropolymers. *Integr. Environ. Assess. Manag.* **14**, 316–334 (2018).
29. Lindquist, G. A. et al. Oxidative instability of ionomers in hydroxide-exchange-membrane water electrolyzers. *Energy Environ. Sci.* **16**, 4373–4387 (2023).
30. Mineart, K. P., Lee, B. & Spontak, R. J. A solvent-vapor approach toward the control of block ionomer morphologies. *Macromolecules* **49**, 3126–3137 (2016).
31. Tang, B. Y., Bisbey, R. P., Lodaya, K. M., Toh, W. L. & Surendranath, Y. Reaction environment impacts charge transfer but not chemical reaction steps in hydrogen evolution catalysis. *Nat. Catal.* **6**, 339–350 (2023).
32. Dinh, H. Q., Toh, W. L., Chu, A. T. & Surendranath, Y. Neutralization short-circuiting with weak electrolytes erodes the efficiency of bipolar membranes. *ACS Appl. Mater. Interfaces* **15**, 4001–4010 (2023).
33. Hohenadel, A., Gangrade, A. S. & Holdcroft, S. Spectroelectrochemical detection of water dissociation in bipolar membranes. *ACS Appl. Mater. Interfaces* **13**, 46125–46133 (2021).
34. Reiter, R. S., White, W. & Ardo, S. Electrochemical characterization of commercial bipolar membranes under electrolyte conditions relevant to solar fuels technologies. *J. Electrochem. Soc.* **163**, H3132 (2016).
35. Mitchell, J. B., Chen, L., Langworthy, K., Fabrizio, K. & Boettcher, S. W. Catalytic proton–hydroxide recombination for forward-bias bipolar membranes. *ACS Energy Lett.* **7**, 3967–3973 (2022).
36. Xu, Q. et al. Integrated reference electrodes in anion-exchange-membrane electrolyzers: impact of stainless-steel gas-diffusion layers and internal mechanical pressure. *ACS Energy Lett.* **6**, 305–312 (2021).
37. Boehm, H. P. Acidic and basic properties of hydroxylated metal oxide surfaces. *Discuss. Faraday Soc.* **52**, 264–275 (1971).
38. Tamura, H., Mita, K., Tanaka, A. & Ito, M. Mechanism of hydroxylation of metal oxide surfaces. *J. Colloid Interface Sci.* **243**, 202–207 (2001).
39. Mueller, R., Kammler, H. K., Wegner, K. & Pratsinis, S. E. OH surface density of SiO_2 and TiO_2 by thermogravimetric analysis. *Langmuir* **19**, 160–165 (2003).
40. Chen, J. et al. Interactions of oxide surfaces with water revealed with solid-state NMR spectroscopy. *J. Am. Chem. Soc.* **142**, 11173–11182 (2020).
41. Wang, G. et al. Hydrogen-treated TiO_2 nanowire arrays for photoelectrochemical water splitting. *Nano Lett.* **11**, 3026–3033 (2011).
42. Fujihara, S. et al. Hydrothermal routes to prepare nanocrystalline mesoporous SnO_2 having high thermal stability. *Langmuir* **20**, 6476–6481 (2004).
43. Sheng, W., Gasteiger, H. A. & Shao-Horn, Y. Hydrogen oxidation and evolution reaction kinetics on platinum: acid vs alkaline electrolytes. *J. Electrochem. Soc.* **157**, B1529 (2010).
44. Schwämmlein, J. N. et al. Origin of superior HOR/HER activity of bimetallic Pt–Ru catalysts in alkaline media identified via Ru@Pt core–shell nanoparticles. *J. Electrochem. Soc.* **165**, H229 (2018).
45. Tongwen, X. Electrodialysis processes with bipolar membranes (EDBM) in environmental protection—a review. *Resour. Conserv. Recycl.* **37**, 1–22 (2002).
46. Bipolar Membrane Electrodialyzer [ACILYZER BPED products]. *ASTOM* http://www.astom-corp.jp/en/product/05.html (2023).
47. Culcasi, A., Gurreri, L., Cipollina, A., Tamburini, A. & Micale, G. A comprehensive multi-scale model for bipolar membrane electrodialysis (BMED). *Chem. Eng. J.* **437**, 135317 (2022).

Methods

BPM electrolyser fabrication

Methods were adapted from our previous work[6,19]. A 16 cm^2 anode gas diffusion layer (GDL) was prepared by spray coating OER-catalyst ink dispersion on stainless-steel fibre mesh (Bekaert Fibre Technologies). The anode catalyst dispersion was prepared as two vials each containing 0.10 g of Co_3O_4 (30–50 nm, US Research Nanomaterials), 0.50 g 18.2 MΩ H_2O, 1.70 g isopropyl alcohol (IPA) and 0.10 g PiperION-A5 ionomer (TP-85, 5% w/w, Versogen) as a suspension. After spraying the catalyst layer, a topcoat (~10% of total catalyst weight) of TP-85 (2% w/w) was sprayed on the GDL. The GDL was cut into 1.0 cm^2 pieces and used separately for each device. The cathode GDL was fabricated by spraying Pt HER catalyst dispersion on Toray Carbon Paper 090 (wet proofed, Fuel Cell Store) to achieve 2.0 mg cm^{-2}. The cathode catalyst ink dispersion contained 0.10 g Pt black (high SA, Fuel Cell Store), 1.50 g 18.2 MΩ H_2O, 1.70 g IPA and 0.10 g D520 Nafion dispersion (alcohol-based 1000 EW at 5 wt%, Fuel Cell Store). Ink containing 25 mg Pt/C powder (20% Pt on Vulcan XC-72R, Fuel Cell Store), 1.00 g 18.2 MΩ H_2O, 1.70 g IPA and 0.10 g D520 Nafion was used for devices with 0.10 mg cm^{-2} Pt loading. A topcoat (~10% of total catalyst weight) of dispersed Nafion D520 (5 wt% alcohol-based) was sprayed on the GDL before it was cut into 1.0 cm^2 pieces and used separately for each device.

Nafion NR212 (50 µm, Ion Power) and PiperION-A40-HCO_3 (40 µm, Versogen) were used as a CEL and AEL, respectively, in the BPMs. The CEL was purchased in a pre-protonated state and was soaked and stored in ultrapure H_2O. The AEL was soaked in 0.50 M KOH for >1 h, stored in fresh 0.50 M KOH and rinsed in 18.2 MΩ water before use. Both membrane layers were cut into 1.2 cm × 1.2 cm squares before use. The WD catalysts were spray coated on top of the CEL. The final active area was 1.0 cm^2. The mother ink of WD catalysts was prepared by sonicating (4 h at room temperature) 0.1 g of catalyst nanoparticles with 4.9 g of 18 MΩ deionized (DI) H_2O. A varied amount of this mother ink was mixed with 0.50 g (total weight with WD catalyst) of 18 MΩ DI H_2O and 1.70 g IPA to prepare the ink for spraying. No ionomer was added to the WD-catalyst ink. The electrolyser setup (PEM fuel-cell hardware, Fuel Cell Store, with a home-made stainless-steel flow field) was assembled using several PET gaskets (McMaster-Carr). The gasket assembly's total thickness at the cathode flow field was maintained at 0.032″ (0.081 cm), while at the anode flow field, it was kept at 0.037″ (0.094 cm). A Ti spacer (Ti frit electroplated with 1 µm Pt, 1.0 cm × 1.0 cm, Baoji Yinggao Metal Materials) was placed beneath the cathode GDL. Different loadings of WD catalyst were coated on the Nafion layer, and the best mass loading was identified from the overall voltage required to drive the water electrolysis at 500 mA cm^{-2}. The η_{wd} of different WD catalysts was measured at the optimal mass loading using the membrane-sensing technique[19]. The combined overpotential of HER and OER was found by subtracting η_{wd} from the cell voltage and water-splitting thermodynamic voltage of 1.23 V. In our experiments, pure water is typically supplied to both the cathode and anode to prevent dry-out from affecting the WD catalysis. However, we observed minimal performance variation between experiments with dry and wet cathodes, as reflected in the polarization curves of the BPM with the optimal WD catalyst in both cases (Supplementary Fig. 14).

Membrane potential sensing

In some cases, a membrane-potential-sensing setup was used[19]. The CEL sensing strip (1.5 cm × 7.5 cm) was placed aligned to one end of the active region on top of the HER GDL. The WD-catalyst-coated CEL was placed on top of the cathode GDL (the uncoated side was in contact with the GDL) touching the CEM sensing strip outside the active region. The BPM was built in the cell by placing the AEL on top of the coated CEL, thereby sandwiching the WD catalyst layer. The AEL sensing strip was placed on top of the AEL side touching the end of the active region. The anode GDL was placed inside the active area on top of the AEL (with the catalyst layer touching the AEL top side), and another Ti spacer was installed at the top. Finally, the flow fields and current collectors were tightened to 50 inch-pounds (5.6 Nm). O-ring joints (9 mm inner diameter, Chemglass) were placed on top of both membrane sensing strips, and the entire assembly was clamped with clips. Hg/HgO and saturated calomel reference electrodes were placed inside the O-ring joint positioned on the AEL and CEL sides, respectively. A schematic of the membrane–electrolyser assembly, including all stacking layers, is provided in Supplementary Fig. 9b. Ultrapure water (18.2 MΩ cm) was circulated from both sides of the electrolyser setup, and η_{wd} was measured at 55 °C in the reverse-bias condition from

$$\eta_{wd} = V_{wd} - V_{wd,eq} = \left(V_{wd}^{raw} + \Delta V_{RE}\right) - \left(V_{wd,eq}^{raw} + \Delta V_{RE}\right) = V_{wd}^{raw} - V_{wd,eq}^{raw} \quad (3)$$

$$V_{wd} = V_{wd}^{raw} + \Delta V_{RE}. \quad (4)$$

Here, V_{wd}^{raw} was the measured voltage between the two reference electrodes, and $\Delta V_{RE} = 0.136$ V is the equilibrium potential difference between the reference electrodes. The term $V_{wd,eq}$ is the electric potential drop measured across the BPM under open-circuit conditions (no current) that thus approaches the equilibrium value[34]. The measured η_{wd} at different current densities was subtracted from the total cell potential to calculate the potential offset required to drive electrolysis without including η_{wd}. The average voltage offset at 500 mA cm^{-2} was calculated by plotting a calibration curve with three commercial catalyst samples: P25-TiO_2, 18 nm SnO_2, R-TiO_2 and a pristine BPM (Supplementary Fig. 9). This average voltage offset was subtracted from the overall cell voltage to estimate η_{wd} for all the other samples reported in Fig. 2. The cathode and anode GDLs were always prepared with the same catalysts, inks and methods to accurately isolate the effect of WD catalyst.

Preparation of 3 nm SnO_2 WD catalyst

A stock solution was prepared by dissolving fresh (hygroscopic) $SnCl_4 \cdot 5H_2O$ (Sigma-Aldrich) in 18.2 MΩ water at room temperature at 0.050 mol l^{-1}. The solution was refluxed at 90–95 °C for 20 min to yield a translucent milky white dispersion and then allowed to cool to ambient temperature. A white precipitate was collected by centrifugation, and the sample was thoroughly washed with water to remove excess salt. The precipitate was stored in a paste-like hydrous condition without drying. The wet/hydrous SnO_2 paste was weighed and then diluted with a water and IPA mixture (1:1 by weight) to obtain various concentration WD catalyst inks. A 1.50 cm^2 square of AEL was taped (at the edge) on a glass slide, and the centre area (1.2 cm × 1.2 cm) was used for spin coating at 3,000 RPM for 30 s after adding drops of the ink to the centre of the AEL until it was fully covered. A solid content of ~2% by weight in the ink proved to be the best loading tested.

Measurement of the loading and thickness of the WD catalyst layer

Lightweight microscope cover slips, coated with a thin ionomer layer, were used as the substrate to measure the mass loading of the WD catalysts. The ink was applied to a cover slip of the same size as the membrane (1.2 cm × 1.2 cm), and the subsequent mass change was measured using a semi-microbalance (Sartorius Quintix). To determine the thickness of the BPM after it is in the cell, the BPM was placed in the same electrolyser cell, gasket assembly and GDL system. The flow fields and current collectors were subsequently tightened to 50 inch-pounds to replicate the water electrolysis environment. The BPM was then removed from the flow field and immersed in a liquid N_2 bath. Following this, the BPM was finely cut inside liquid N_2, and cross-sectional electron microscopy (Thermo Scientific, Apreo) was performed to determine the thickness.

Preparation of hydrocarbon CEL

SPEEK random copolymer was provided by eSpin Technologies. To synthesize the SPEEK, poly(ether-ether ketone) (PEEK) was reacted with concentrated aqueous H_2SO_4 in an overhead stirrer at 90 °C for 4 h. Ice-cold

water was used to precipitate the sulfonated PEEK (SPEEK), which was then washed thoroughly to remove unreacted acid. The washed polymer was dried in an oven at 60 °C, and SPEEK was cast to form a 30 (±5) μm film using a wet film applicator. A second hydrocarbon-based membrane, TESET block copolymer (52 mol% midblock sulfonation), was also tested as a replacement for Nafion. Full details of the preparation of the TESET film are given elsewhere[30,48]. The TESET copolymer, commercially known as NEXAR, was provided in sulfonated form by the Kraton Corporation. The polymer was dissolved in a toluene:IPA 85:15 v:v mixture at ambient temperature to make a 4.0 wt% solution. Films measuring 35 ± 5 μm were cast in a Teflon mould. The solvent was evaporated for 3 days, and the resulting films were vacuum-dried at ambient temperature for 24 h.

Reference AEM electrolyser assembly

The anode ink and GDL were prepared identically as described above for the BPMWE. For the alkaline cathode, 0.10 g PiperION-A5 ionomer (TP-85, 5% w/w) was used to prepare the catalyst ink. The loading for high- and low-Pt experiments was maintained as 2.0 and 0.10 mg cm^{-2}, respectively. A topcoat (~10% of total catalyst weight) of TP-85 (2% by weight) was sprayed on the GDL, and it was cut to 1.0 cm^2 pieces.

Electrodialysis environment testing

Electrolytes of 0.1 M H_2SO_4 and KOH were used as catholyte and anolyte instead of DI water. Currento 2Ni18-0.50 (Bekaert Fibre Technologies) was used as the anode GDL instead of stainless steel to prevent corrosion, observed in the presence of KOH electrolyte feed to the anode. All the other parameters were identical to the BPMWE.

Data availability

The data generated from this study and used to prepare the figures in the main manuscript are available with the digital identifier (https://doi.org/10.6084/m9.figshare.25769388). Further datasets generated during the study are available from the corresponding author on reasonable request. Source data are provided with this paper.

References

48. Mineart, K. P., Jiang, X., Jinnai, H., Takahara, A. & Spontak, R. J. Morphological investigation of midblock-sulfonated block ionomers prepared from solvents differing in polarity. *Macromol. Rapid Commun.* **36**, 432–438 (2015).

Acknowledgements

The work investigating WD catalyst descriptors was supported by the US Office of Naval Research, grant N00014-20-1-2517 (S.W.B.). The design of the new high-performance catalyst was supported by US Advanced Research Projects Agency-Energy (ARPA-E), grant DE-AR0001502. The work applying the new catalyst to electrodialysis and with hydrocarbon cation-exchange membrane layers was supported by ARPA-E grant DE-AR0001540. P.V.S. acknowledges the Fulbright-Nehru postdoctoral fellowship supported by USIEF. K.M.W. and R.J.S. acknowledge support from the Kraton Corporation and the NC State College of Engineering. We acknowledge use of shared instrumentation in the Center for Advanced Materials Characterization in Oregon and the Phil and Penny Knight Campus. J. Razink collected electron-microscopy images. R. Wycisk and J. Doshi at eSpin Technologies are acknowledged for providing SPEEK membranes and for useful technical discussion.

Author contributions

S.S. and S.W.B. conceived the experiments and led the project. S.S. performed most experiments. L.C. developed membrane-sensing experiments and data processing approaches. P.V.S. led the AEM and low-Pt BPM experiments. O.T.V. conceived the thickness measurements and assisted in the BPMED prototype experiment. C.R.S. performed the NMR experiments. K.M.W. and R.J.S. initiated discussions regarding and developed the TESET membrane. S.S. and S.W.B. wrote the manuscript with input from all authors.

Competing interests

The authors have filed a patent application titled 'Dissociation and recombination catalyst layers for reverse and forward-bias bipolar membranes' (US20230264148A1), on materials reported in this manuscript and are working to commercialize advanced BPMs.

Additional information

Supplementary information The online version contains supplementary material available at https://doi.org/10.1038/s41563-024-01943-8.

Correspondence and requests for materials should be addressed to Shannon W. Boettcher.

Peer review information *Nature Materials* thanks Christopher G. Arges, Severin Vierrath and the other, anonymous, reviewer(s) for their contribution to the peer review of this work.